nature materials

SUPPLEMENTARY INFORMATION

https://doi.org/10.1038/s41563-018-0182-6

In the format provided by the authors and unedited.

Injectable tissue integrating networks from recombinant polypeptides with tunable order

Stefan Roberts[1], Tyler S. Harmon[2,3], Jeffrey L. Schaal[1], Vincent Miao[1], Kan (Jonathan) Li[4], Andrew Hunt[1], Yi Wen[1], Terrence G. Oas[4], Joel H. Collier[1], Rohit V. Pappu[3] and Ashutosh Chilkoti[1]*

[1]Department of Biomedical Engineering, Duke University, Durham, NC, USA. [2]Department of Physics, Washington University in St. Louis, St. Louis, MO, USA. [3]Department of Biomedical Engineering and Center for Biological Systems Engineering , Washington University in St. Louis, St. Louis, MO, USA. [4]Department of Biochemistry, Duke University, Durham, NC, USA. *e-mail: chilkoti@duke.edu

Supplementary Information

Injectable tissue integrating networks from recombinant polypeptides with tunable order

Stefan Roberts[1], Tyler S. Harmon[2,4], Jeffery Schaal[1], Vincent Miao[1], Kan (Jonathan) Li[3], Andrew Hunt[1], Yi Wen[1], Terrence G. Oas[3], Joel H. Collier[1], Rohit V. Pappu[4], Ashutosh Chilkoti[1]*

Affiliations:

[1]Department of Biomedical Engineering, Duke University, Durham, North Carolina, 27708, USA

[2]Department of Physics, Washington University in St. Louis, St. Louis, Missouri 63130, USA

[3]Department of Biochemistry, Duke University, Durham, North Carolina, 27708, USA

[4]Department of Biomedical Engineering and Center for Biological Systems Engineering, Washington University in St. Louis, St. Louis, Missouri 63130, USA

*__Corresponding Author__: Ashutosh Chilkoti: chilkoti@duke.edu

Supplementary Information

Supplementary Methods and Discussion:

Secondary Structure analysis

Given the prevalence of beta turns within ELPs and the possibility of polyalanine forming beta structures, helicity was initially quantified using BeStSel (Supplementary Table 2)[1], a deconvoluation algorithm targeted at more complicated beta structures. As others have noted[2,3], however, the deconvolution of CD spectra is particularly sensitive to the choice of basis sets and algorithm, especially with disordered and beta-turn conformation—both highly present in our polymer system. We included the CD data and the deconvolution for reference but consider these results more qualitative than quantitative. As a result, we also conducted NMR on POPs to better determine the quantitative amount of helicity present in each polymer.

For NMR, polymers were grown in M9 minimal media with ^{15}N-NH_4Cl and ^{13}C-Glucose (Cambridge Isotopes, Tewksbury, MA) as the only nitrogen and carbon sources to ensure protein labeling. Samples were prepared in PBS (pH=7.4) unless otherwise noted. All NMR spectra were collected on an INOVA 600 (Varian Instruments, Palo Alto, CA) spectrometer with a triple resonance cryoprobe equipped with a z-field gradient coil. Though the repetitive and proline rich nature of POPs increases the complexity of resonance assignments, identifying key amino acids was enabled by combinations of triple resonance NMR spectra (Supplementary Figure 3). Resonance assignments were made using a set of triple resonance experiments including HNCO, HN(CA)CO, HN(CO)CA, HNCA, HCAN, and HCA(CO)N. The NMR spectra were processed using NMRpipe[4], and were analyzed using NMRviewJ. Chemical shifts in the proton dimension were referenced relative to TMSP (trimethylsilylpropanoic acid) as 0 ppm. Quantification of helicity was accomplished using the identified alanine peaks of the H(N)CO spectra for E1-H2-25%. Chemical shift positions were placed on a spectrum of values ranging from fully disordered

(177.19 ppm) to fully helical (180.78 ppm), as determined Vendruscolo *et al*.[5,6] and the central alanine peak of the 15˚C H(N)CO respectively, producing the values in Supplementary Table 3. The method to calculate helicity was adapted from the δ2D algorithm developed by Vendruscolo *et al*.[6] Alanine residues corresponding to carbon chemical shifts of peaks 2-7 were designated as fringe amino acids at the edges of the helix. This designation is consistent with predictions based on helix-coil transition theory in which 6 alanine residues occur at values lower than the core set. All other alanine residues were assumed to be in the helical core. A subsequent averaging of the helicity values produces a helicity for each H2 polyalanine domain of 91%. The high degree of helicity is further supported by helix-coil transition theory[7,8] and the temperature dependent change of the chemical shifts of backbone carbonyl carbons (Supplementary Table 3).

Coarse-grained molecular dynamics simulations

We developed a coarse-grained bead-tether model for the POPs. The design of the model is based on phenomenological considerations and computational complexity. It is important to be able to include $O(10^3)$ molecules in each simulation run if we are to capture the interplay between dispersed and aggregated phases at different conditions. This requires simple, short-range potentials and a tractable number of interaction sites per molecule. The numbers of beads for the polyalanine versus ELP modules were chosen based on considerations of effective solvation volumes as previously described for other systematically coarse-grained systems[9,10]. The dimensions of a single pentapeptide repeat of an ELP do not vary significantly with temperature in atomistic simulations that were performed using the ABSINTH implicit solvation model[11,12]. Similarly, the dimensions of individual polyalanine pentapeptides are also temperature independent and they are roughly equivalent to that of an ELP pentapeptide. These observations are concordant with the designation of thermal blobs spanning roughly 5-7 residues in generic

polypeptide sequences[13,14]. Accordingly, each ELP repeat and pentapeptide polyalanine segments were modeled using beads of similar sizes.

In the bead-tether model the covalent bonds were modeled using a harmonic potential with spring constants of 2 kcal/mol/Å^2 and an equilibrium distance of 10 Å. Bond angle restraints at the junctions of pairs of bonds were modeled using angular potentials with spring constants of 1 kcal/mol/radian^2 and equilibrium angles of 180 and 150 degrees for the alanine and ELP beads, respectively. These values capture the geometries corresponding to polyalanine helices and randomly coiling ELPs. We modeled all non-covalent interactions amongst ELP and polyalanine beads using pair potentials based on the 12-6 Lennard-Jones (LJ) model. The ELP and polyalanine beads have identical hard-core diameters of 6 Å. The distinctions between interactions involving ELP versus polyalanine beads were modeled into the choices we made for the well-depth parameter of the LJ potentials. We chose the interaction strengths of the ELP beads such that this range would span from highly soluble to aggregating polymers. This was quantified by running simulations with a range of energies and after equilibrating for 100 ns, decreasing these interaction strengths by 0.05 kcal/mol every 25 ns. We quantified the number of polymers in the largest cluster, where two proteins are interacting if two beads were within 8 Å, as a proxy for aggregation versus solubility in our simulations. These polymers were strongly aggregating for interaction strengths of 0.35 kcal/mol and readily disaggregated when the interaction energies dropped to 0.25 kcal/mol. Accordingly, we used a range of interactions strengths for the ELPs that spanned at least 0.05 kcal/mol to 0.40 kcal/mol. This range of interaction strengths is our way of modeling the impact of increasing temperature from below the LCST to above the LCST. We used a similar technique to parameterize the interactions between polyalanine beads. Here, the prescription for choosing suitable interaction strengths was based on being able to observe a clear tendency for

aggregation of polyalanine domains. Accordingly, we used interaction strengths of at least 1kcal/mol for interactions amongst the alanine beads.

Hysteretic effects were diagnosed by the presence of path dependencies in the evolution of specific order parameters as a function of heating versus cooling, which in the simulations will be observed by tuning the strengths of ELP interactions. To test for effects related to hysteresis we utilized two different sets of initial conditions. The first scheme, designated as the dimer initial conditions, was designed to create states that we hypothesize as being representative of the pathway that the system will pass through as it approaches the LCST from below. Simulations of two proteins were equilibrated for 100 ns in a simulation box of 250 Å. This allowed the alanine domains in dimers to pre-aggregate into a core. We then utilized 25 conformations drawn at random from the ensemble of dimers to initialize simulations of the full system. These dimers were placed in the simulation with a randomly chosen translational offset while ensuring against steric clashes. At high ELP interaction strengths the molecules dock against one another. In these morphologies, the ELPs exposed to solvent while forming a corona around the polyalanine cores now dock against one another to minimize the ELP-solvent interface. Additionally, there is a thermodynamic driving force for the merger of polyalanine cores leading to the formation of clusters with larger cores, yielding the thermodynamically optimal radius for clusters.

The second scheme, which we designate as the coil initial conditions, was designed to create a thermodynamically equilibrated aggregate. In this setup, we started the simulation with each polymer conformation being generated randomly. The only correction was to prevent steric clashes. These simulations showed a rapid initial collapse as the polyalanine domains find one another. Additionally, above the LCST ELP domains collapse and self-associate as well. These simulations converged toward conformations with clusters of alanine domains that were well

connected. After equilibrating for 100 ns, the interaction strength of the ELPs were decreased by 0.10 kcal/mol every 25 ns to model crossing from above the LCST to below the LCST. These simulations showed swelling as the ELPs no longer favored being in a high density but the connectivity of alanine domains between the two domains prevented the system from separating. The main text shows a graphical summary to summarize the main findings from the coarse-grained simulations. A detailed quantitative analysis of the simulation results and an accompanying phenomenological model will be introduced in follow-up studies that build on experiments designed to test the main tenets of the findings summarized in Figure 3.

In all of our simulations, we used spherical droplets instead of large cubic cells with periodic boundaries. This choice was mandated by several considerations: In simulations with cubic geometries for the central simulation cells and periodic boundary conditions, the POP proteins rapidly formed alanine clusters as the alanine domains found other alanine domains that were in close proximity. This behavior is similar to what is observed in simulations with spherical boundary conditions. The key distinction is with regard to assessments of network formation between the two categories of simulations. In simulations using spherical droplets, the entire network collapses due to ELP:ELP interactions and the assessment of phase separation becomes relatively straightforward due to our ability to use the incorporation of molecules into the single largest, system-spanning cluster as a proxy for phase separation in a finite-sized system[9]. However, in simulations based on periodic boundary conditions the networks become disjointed within the central simulation cell, because the system-spanning networks form via interactions with images due to periodic boundary conditions. This creates a periodic boundary artifact that prevents the system from collapsing for physically unrealistic reasons and also hinders the easy use of networking as a useful order parameter for assessments of phase separation. Given these

artifacts and difficulties with analysis, we used spherical droplets as the optimal geometries for simulations of phase separation. This is in accord with well-established simulation literature showing that systems with periodic boundaries give rise confounding artifacts when the systems are heterogeneous, where the heterogeneities arise from density inhomogeneities or inhomogeneities due to the presence of multiple components.

Flow Cytometry

Excised right hind injections (n=3-4) were transferred to 2ml PBS and digested with 0.5mg/ml Collagenase IV (Sigma, St. Louis, MO) and 50 units of DNase I (Sigma, St. Louis, MO) at 37˚C for 45min. Digested tissue was filtered through a 70μm cell strainer and repeatedly washed with sterile 2% FBS (Thermo Fisher, Waltham, MA) in PBS. After ACK (Thermo Fisher, Waltham, MA) lysis, cells were counted using a hemocytometer. Cells were stained as previously described by others[15]. Briefly, cells were blocked with 2.4 G2 antibody (BD Biosciences, San Jose, CA) and stained with anti-mouse CD45-BV-510 (30-F11, BD Biosciences, San Jose, CA), F4/80-PerCP-Cy5.5 (BM8, Biolegend, San Diego, CA), CD11b-APC (M1/70, Biolegend, San Diego, CA), Ly6C-FITC (AL-21 Biolegend, San Diego, CA), Ly6G-PE (IA8, Biolegend, San Diego, CA), CD31-PE-Cy7 (390, Biolegend, San Diego, CA), CD326-APC-Cy7 (G8.8, Biolegend, San Diego, CA), and DAPI (Biolegend, San Diego, CA). All antibodies were diluted 160x from stock concentrations for staining. Cell subtypes were defined as: neutrophils (CD45+ CD11b+ Ly6C+ Ly6G+ F4/80-), inflammatory monocytes (CD45+, CD11b+ F4/80+ Ly6C+ Ly6G-), tissue macrophages (CD45+ CD11b+ F4/80+ Ly6C- Ly6G-), endothelial cells (CD45- CD31+ CD326-), and epithelial cells (CD45- CD326+ CD31-). Cell type analysis was done on a FACSCANTO II (BD Biosciences, San Jose, CA) with a minimum of 50000 live cells analyzed for each sample. AbC anti-rat antibody control beads (Thermo Fisher, Waltham, MA) were used as compensation

controls for all antibody dyes, and a 1:1 mixture of live and dead cells was used as a compensation control for DAPI. Gating procedures are shown in Supplementary Figure 13. Flow cytometry data was gated and quantified with FlowJo (FlowJo LLC, Portland, Oregon) and exported for analysis.

Chemical Crosslinking

POP assembly and stability is derived from physical crosslinks from helical domain swapping, but this method of crosslinking does not preclude the use of additional chemical crosslinking techniques to further modulate mechanical properties. As several POP helices contain at least one lysine, an amine reactive crosslinker was easily incorporated by covalent conjugation. POP aggregates chemically crosslinked with Tetrakis(hydroxymethyl)phosphonium chloride (THPC) show a 2-fold increase in stiffness. For comparison with a fully disordered ELP, we also synthesized E1$(DK)_{80}$, a $(VPGVG)_n$ based polymer with aspartic acid (D) and lysine (K) spaced equivalently to an E1-H5-25% POP (Supplementary Table 1). Chemically crosslinking E1$(DK)_{80}$ also increases its stiffness, though its G' remains an order of magnitude lower than both physically and chemically crosslinked POPs (Supplementary Figure 9). The resultant mechanical properties from chemical crosslinking are lower than that reported by us and others for chemically crosslinked ELPs[16,17] due to the low crosslinking density in E1$(DK)_{80}$ (4 sites/polymer). As previous work has shown that disordered polymers can achieve high stiffness with sufficient crosslinking densities[16,18,19], even stiffer POPs are likely possible should the disordered domain be substituted for one with a high density of chemical crosslinking sites. The use of chemical crosslinking with ELPs does produce a type of interconnected network; however the method of formation and the resultant architecture are distinct from that of physically crosslinked POPs. In essence, the addition of chemical crosslinker to E1$(DK)_{80}$ will arrest coalescence, resulting in an architecture that is a time-dependent snapshot of coacervation (Supplementary Figure 13).

Supplementary Figures

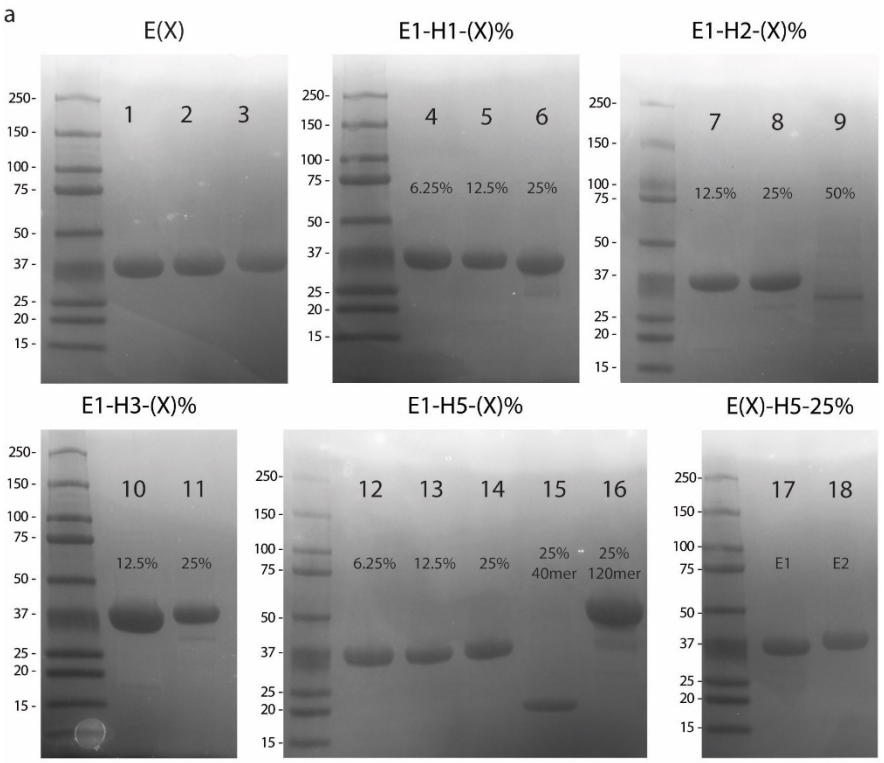

Polymer	Lane
(E1)80	1
(E2)80	2
(E3)80	3
E1-H1-6.25%	4
E1-H1-12.5%	5
E1-H1-25%	6
E1-H2-12.5%	7
E1-H2-25%	8
E1-H2-50%	9
E1-H3-12.5%	10
E1-H3-25%	11
E1-H5-6.25%	12
E1-H5-12.5%	13
E1-H5-25%	14
E1-H5-25%-40mer	15
E1-H5-25%-120mer	16
E2-H5-25%	17
E3-H5-25%	18

Supplementary Figure 1: Purity of POPs (a) All POPs, listed in (b), were purified to >95% as determined by SDS-PAGE gels. (c) The MW of E1-H5-25% was confirmed by MALDI and is within 1.5% of the predicted MW. Small bands observed in the SDS-PAGE are also confirmed to be truncation products of the longer polymer, likely the result of ribosomal pausing. The presence of small amounts of truncation product did not have discernable effects on the properties of POPs.

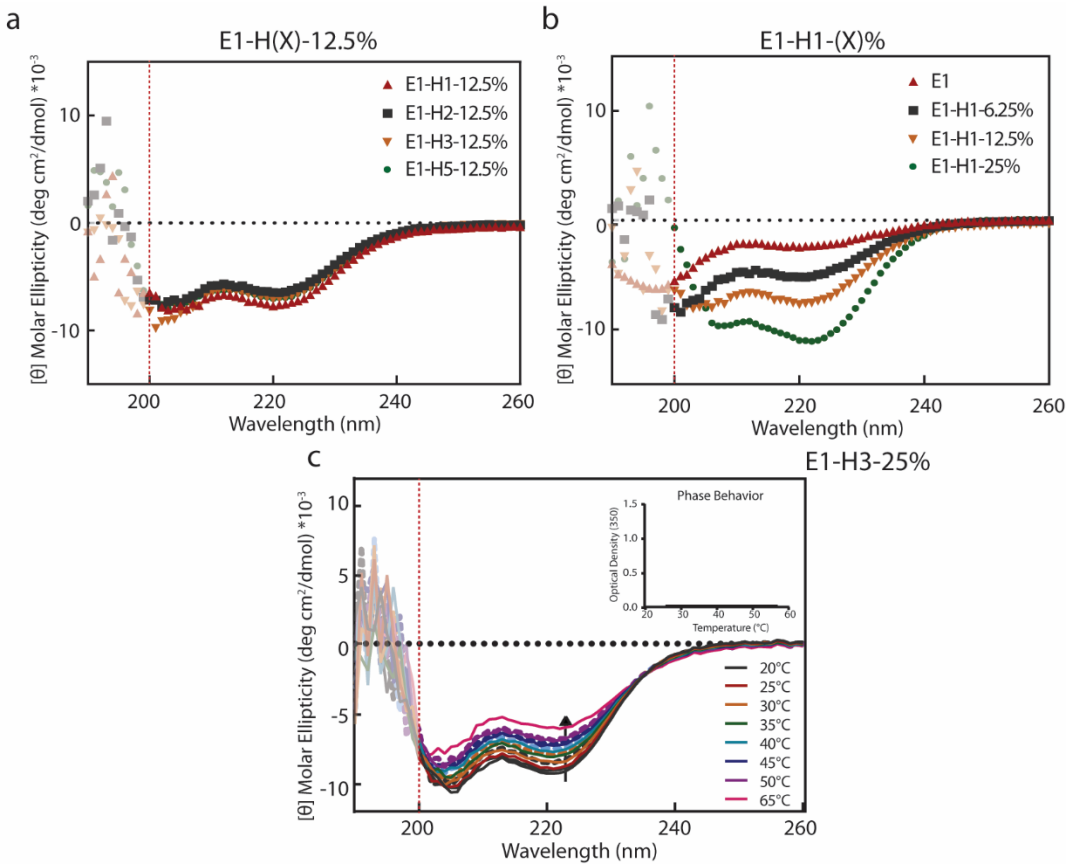

Supplementary Figure 2: Secondary structure characterization by CD spectroscopy of (a) 12.5% oligoalalanine POPs show characteristic peaks at 208 and 222 nm, with all polyalanine domains showing similar peak amplitudes at 222 nm. (b) Peak amplitudes scale appropriately with the inclusion of helical domains for E1-H1 polymers. (c) E1-H3-25%, which does not transition at low temperatures, shows the preservation of helical signature peaks at high temperatures with some loss in peak amplitudes. (Data were not used for analysis when dynode voltage >500 V at <200nm).

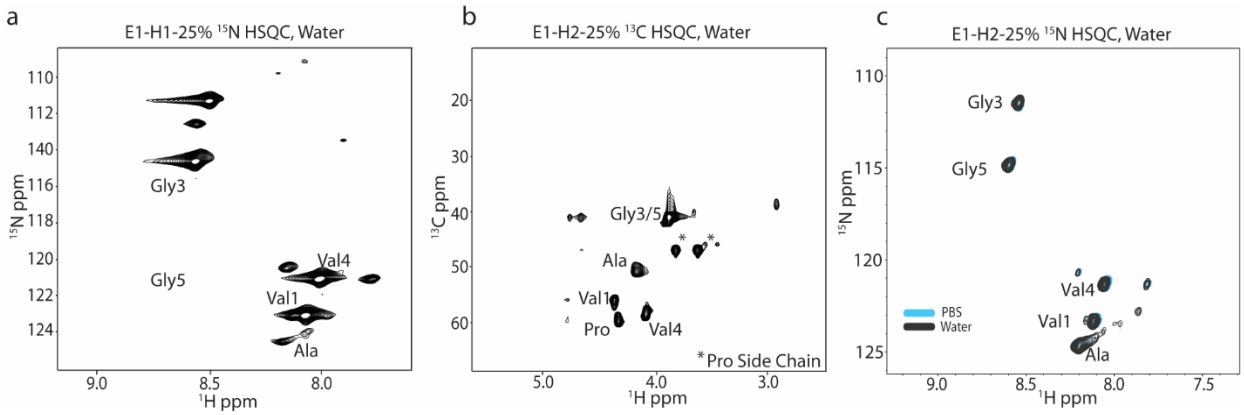

Supplementary Figure 3: Additional NMR analysis (a) The ^{15}N-HSQC spectrum for E1-H1-25% and (b) the ^{13}C-HSQC spectrum for E1-H2-25% show the identifiable amino acid peaks despite the repetitiveness of the polymers (c) The addition salts in PBS does not appreciably alter the chemical shift positions for the polymers.

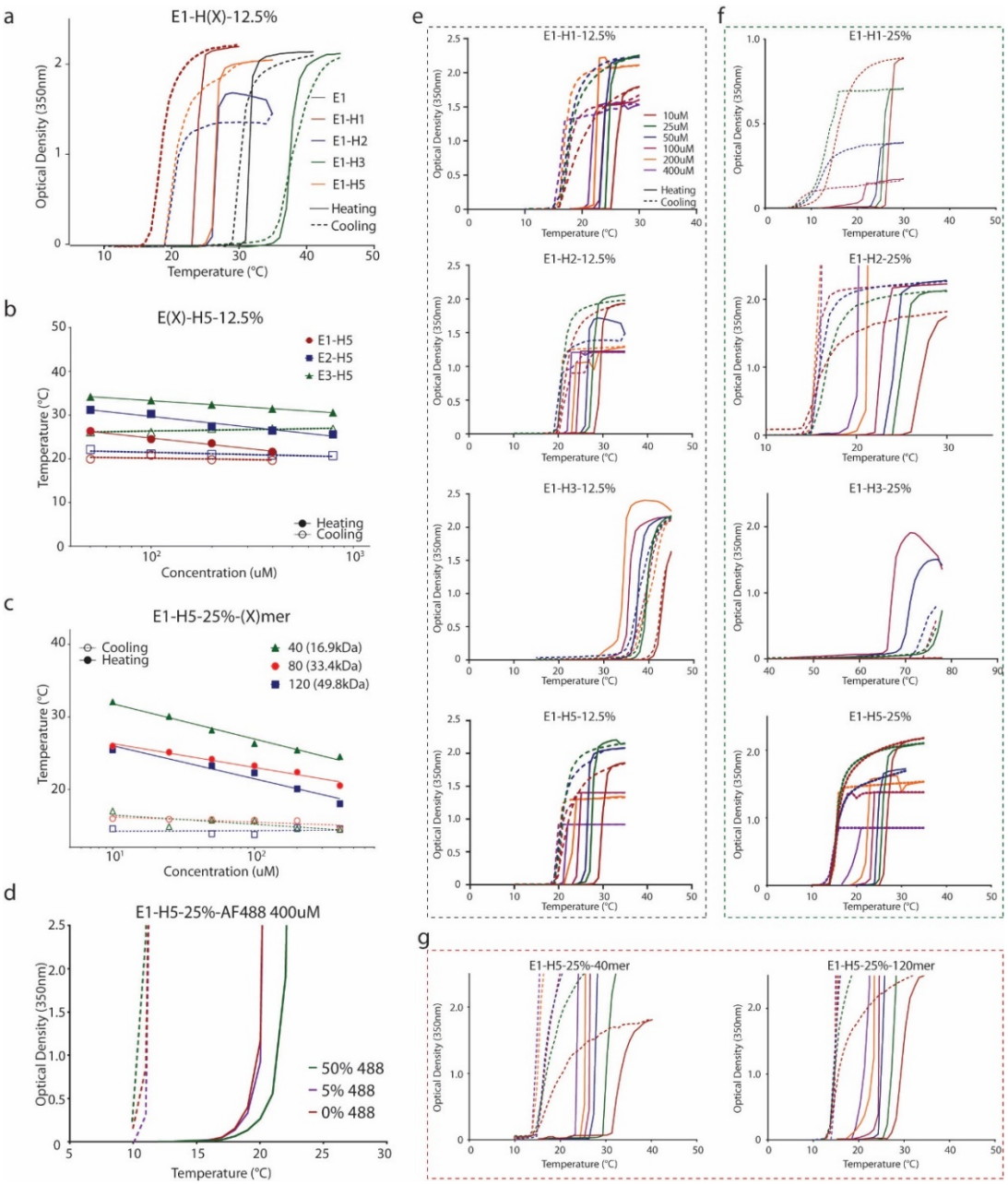

Supplementary Figure 4: Additional optical density (OD) data (a) 12.5% POPs also show variability in hysteresis due to helix composition as well as (b) concentration independence and a tunable T_t-heating. (c) T_t-heating can be tuned by changing molecular weight without changing the total percentage of helicity, though T_t-cooling remains unaltered. (d) Attachment of Alexa Fluor 488 to the lysine residues on POPs does not significantly alter their phase behavior. Raw optical density measurements for (e) E1-H(X)-12.5% polymers, (f) E1-H(X)-25% polymers, and (g) E1-H5-25% of different molecular weights illustrate their sharp phase behavior and varying degrees of hysteresis. Only E1-H1-25% displayed slightly divergent behavior with concentrations >200 μM transitioning too gradually to determine a specific T_t. OD measurements were taken in PBS. Heating and cooling rates were kept at 1°C/min. OD amplitudes are non-interpretable due to differences in aggregate formation, settling, and detector saturation.

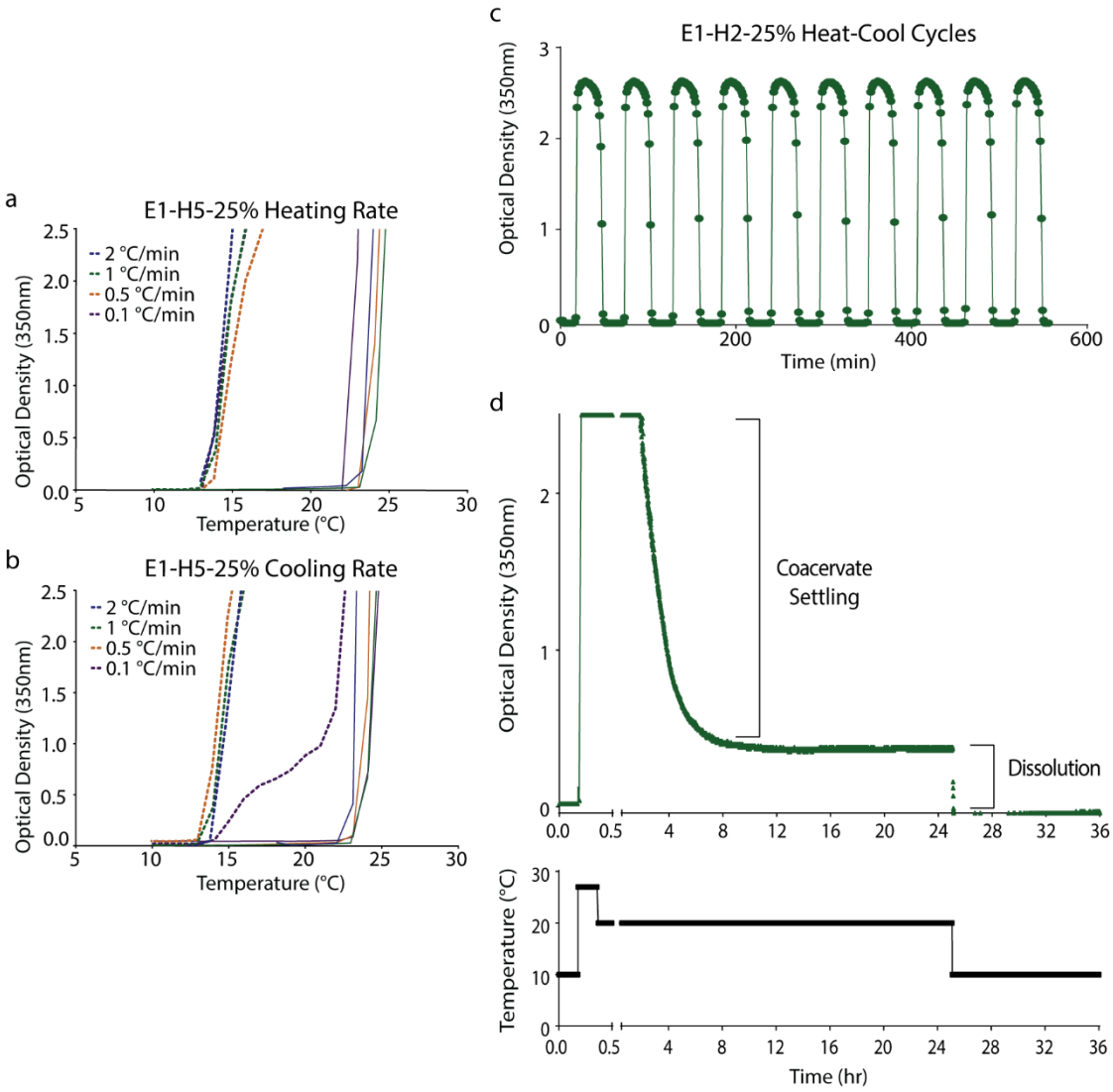

Supplementary Figure 5: Kinetics of hysteresis Altering the (a) heating rates and (b) cooling rates also does not change the phase behavior, though some settling occurs at slower cooling rates. (c) Despite their hysteretic nature, polymers are capable of fully recovering from heating and cooling cycles. Ten cycles show no change in transition temperatures. (d) E1-H5-25% (50 μM, PBS) shows no recovery for 24 h when heated and cooled to the hysteretic range above the T_t-cooling. Subsequent cooling after 24 h shows rapid dissolution.

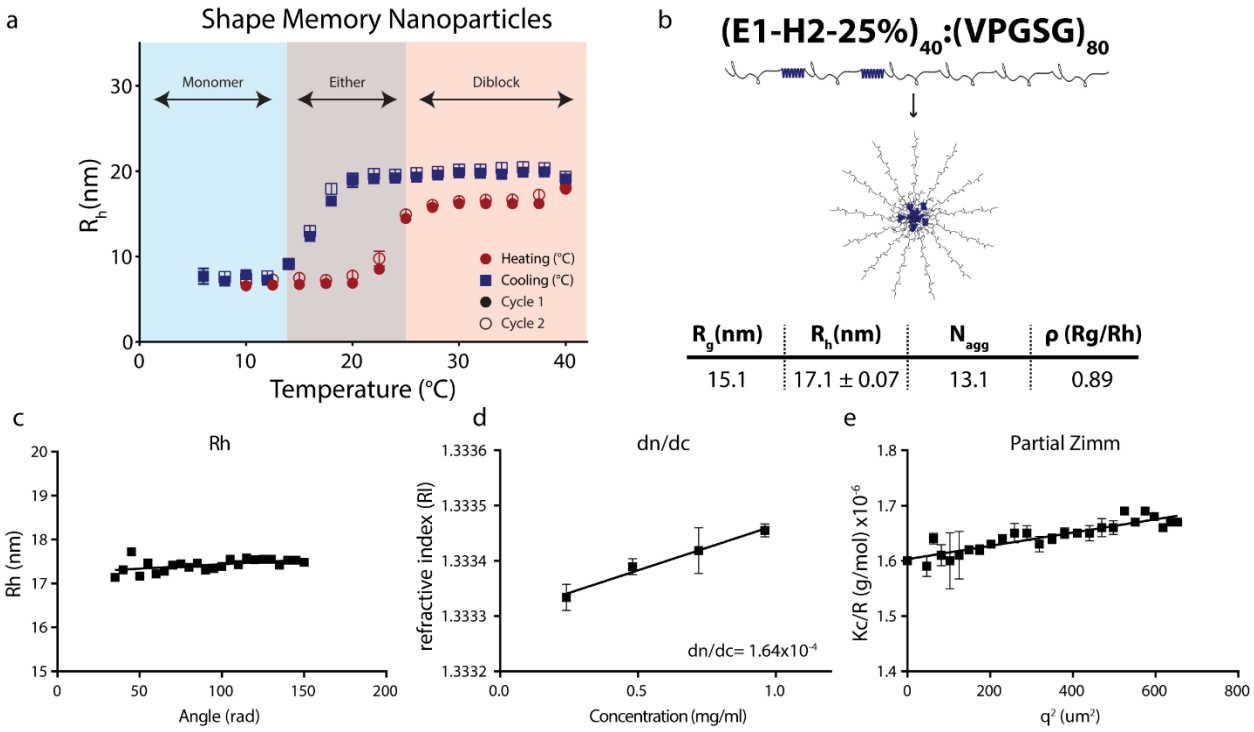

Supplementary Figure 6: Shape memory nanoparticles with POPs (a,b) Diblocks of E1-H2-25% (40mer) with a hydrophilic ELP, $(VPGSG)_{80}$ are soluble unimers below the T_t of the POP core block, and form small micelles ~20nm large when heated. When cooled, the particles retain their size through the hysteretic range, eventually resolubilizing below the POP T_t-cool. The process can be cycled without change to particle size or reversibility; data is either mean or mean ± SD (c) R_h as a function of angle was extrapolated to 0 for reported R_h. (d) The change in refractive index with concentration was used to calculate dn/dc for use in (e) the partial Zimm plot. Analysis was done with a combination of dynamic and static light scattering (PBS, 20µM); data represents mean ± SD (n=3 independent preparations).

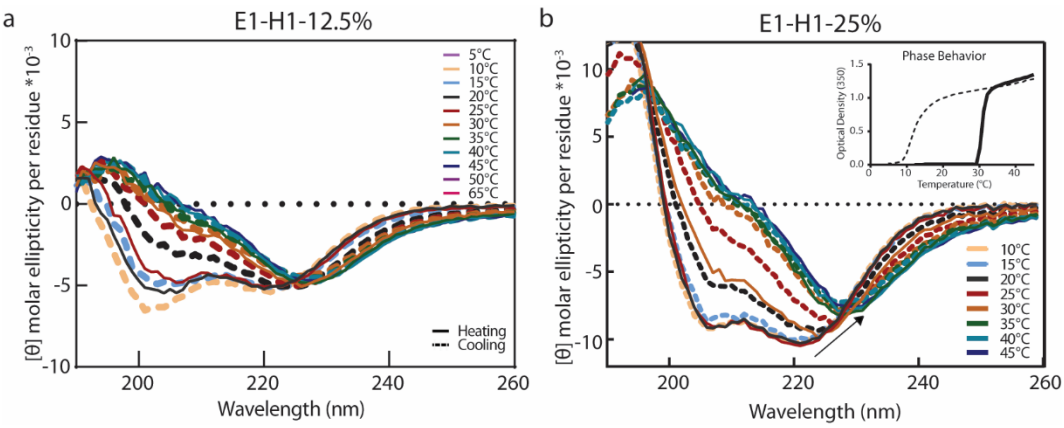

Supplementary Figure 7: Temperature dependent CD (a-b) E1-H1-25% shows a spectral shift consistent with distortions for helical peptides at the expected transition temperature. This polymer also shows an isodichroic point at 225 nm for both 12.5 and 25% E1-H1 polymers. Samples were at 10 μM in water, and a 1 mm path length cuvette was used for all CD measurements. Dynode voltage <500 V for all.

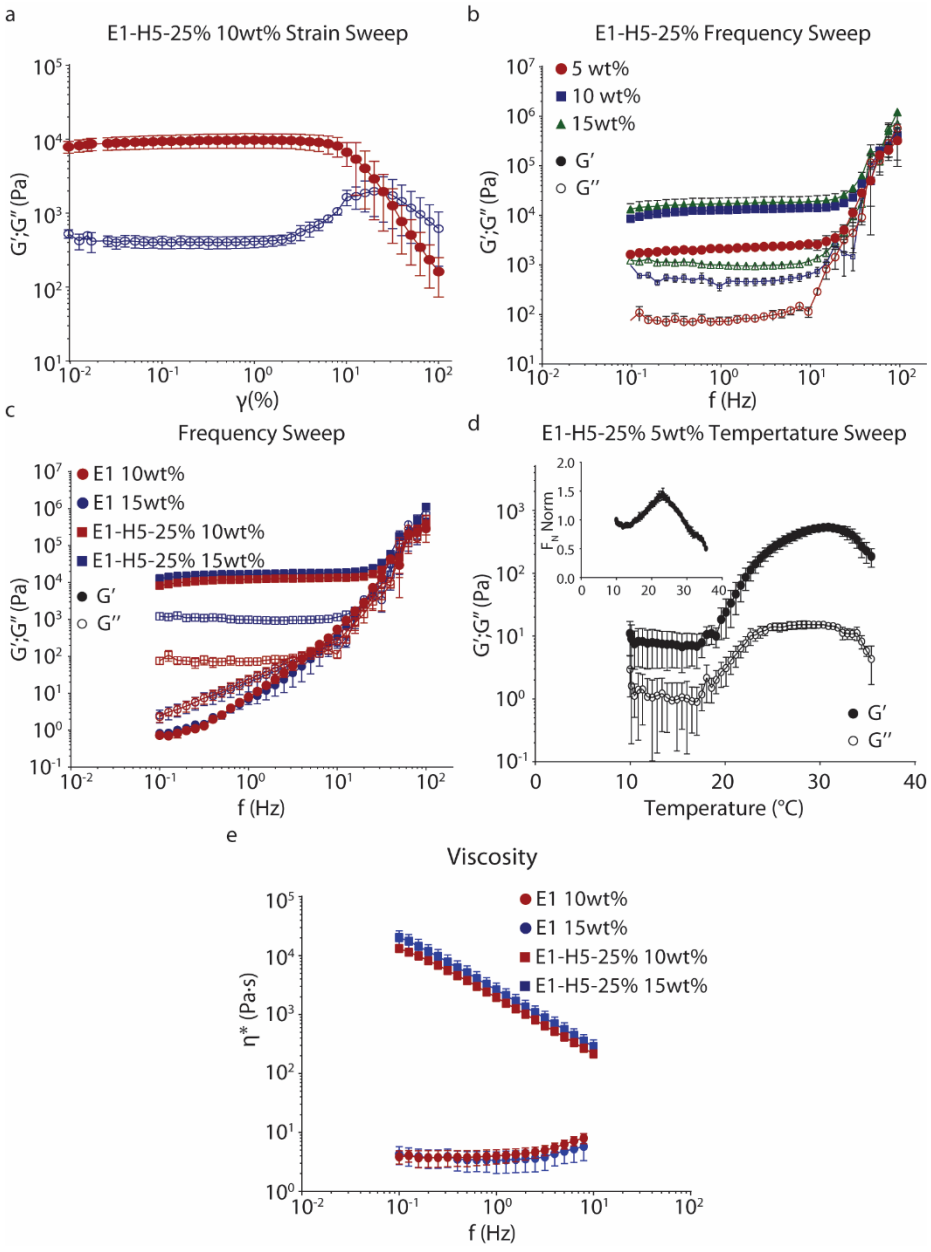

Supplementary Figure 8: Rheology (a) A strain sweep from 0.01 to 100% reveals the linear viscoelastic region (LVER) of POPs. (b) Frequency sweeps within the LVER (1% strain) reveal solid-like material properties for POPs which scale non-linearly with concentration. (c) ELPs show more liquid-like behavior (G"">G') and decrease mechanical integrity compared to POPs. (d) Temperature sweeps of E1-H5-25% show an increase in elastic moduli as the polymer aggregates. The G' plateau and drop-off after transition is due to aggregate shrinking—common for all elastin biopolymers with temperature—and loss of contact with the plates. The change in normal force (F_N) (inset) reflects this loss of contact. (e) POPs exhibit plastic, frequency dependent viscosity whereas ELPs behave as Newtonian fluids. All measurements, except the temperature sweep, were taken after a 30 min equilibration at 37°C. All polymers solubilized in PBS. For all measurements, data represent mean ± SEM (n=3 independent samples).

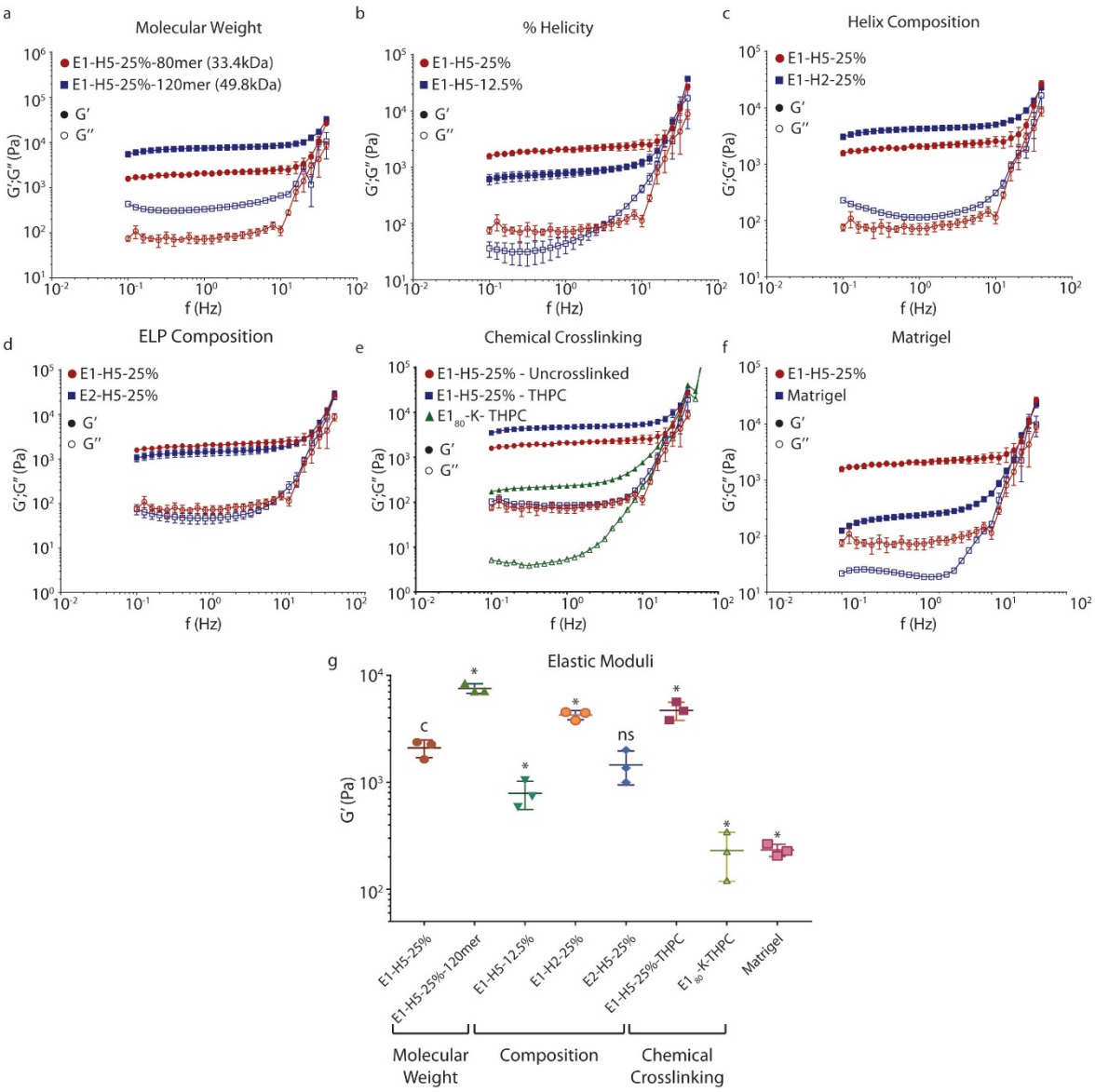

Supplementary Figure 9: Methods of altering mechanical stability (a) Increasing polymer molecular weight or (b) the total polymer helicity increases mechanical stiffness. (c) Helix composition has a significant effect on G', whereas the effect of (d) changing ELP composition is not as dramatic. (e) POP physical crosslinking can be combined with chemical crosslinking. Here we used a lysine crosslinker tetrakis(hydroxymethyl)phosphonium chloride (THPC) at a 4:1 or 1:1 molar ratio of crosslinker to lysine residues. The addition of a chemical crosslinker predictably increases the elastic moduli. Using $E1(DK)_{80}$, an ELP with equal number and equivalently spaced lysine residues (see Supplementary Table 1) to E1-H5-25%, we also show that chemical crosslinking increases ELP stability, though not to the same degree as POPs. (f) Matrigel also behaves as a solid, but soft gel. For a-e, data represent mean ± SEM (n=3 independent samples). (g) The G' at 1% stain and 1Hz were compared to E1-H5-25%, and all polymers showed statistically different mechanical properties except the change in ELP composition; * for $p<0.05$ determined by ANOVA with a Dunnett's post hoc test comparing each to E1-H5-25% as a control ('C'); data are presented as 10-90% box plots with a median central element (n=3 independent samples). All polymers were tested at 5wt% in PBS with 30 min equilibrations at 37°C prior to oscillations.

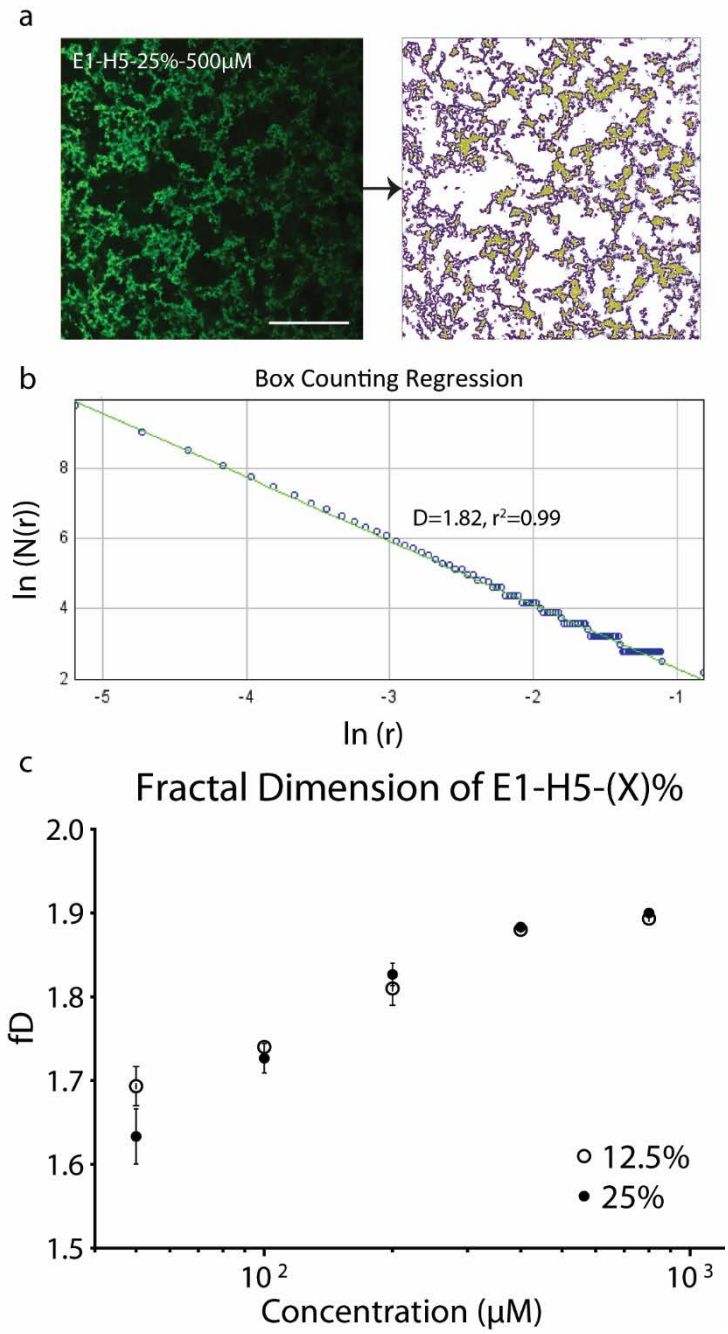

Supplementary Figure 10: Fractal dimensions of POP networks (a) Single plane confocal images of E1-H5-25% in PBS were analyzed using a box counting algorithm in FracLac for ImageJ. (b) The fractal dimension (D) was determined graphically (n=99 for determination of r^2) (c) Images for E1-H5-12.5% and 25% revealed fractal dimensions ranging from 1.6 to 1.9 and varying with concentration data represent mean ± SEM (n=3 independent samples).

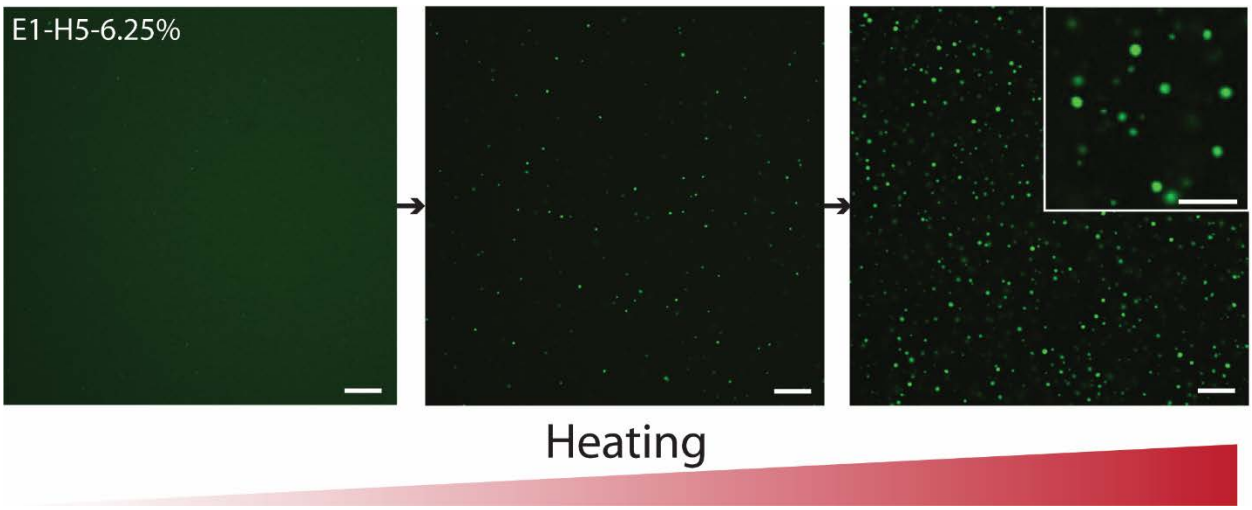

Supplementary Figure 11: Single helix polymer coacervates (all) E1-H5-6.25% (200μM, PBS), which contains only one helical domain per polymer, does not form a fractal network; rather, the polymer forms a colloidal suspension of coacervates, similar to that of ELP. Scale bars = 20μm, 10μm for insert.

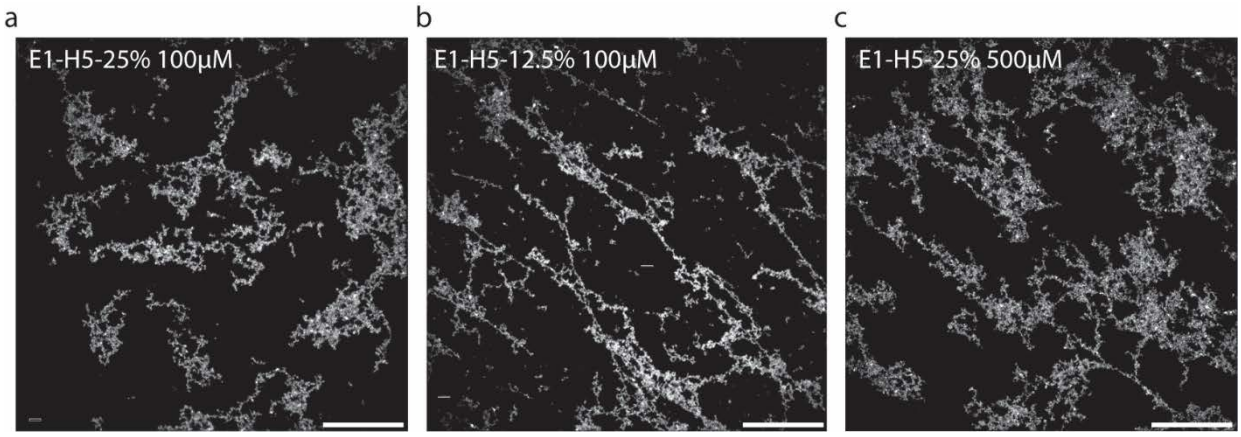

Supplementary Figure 12: Additional SIM images (all) The mesoscale architecture of POPs is consistent across concentrations and helical percentages; scale bar 10μm.

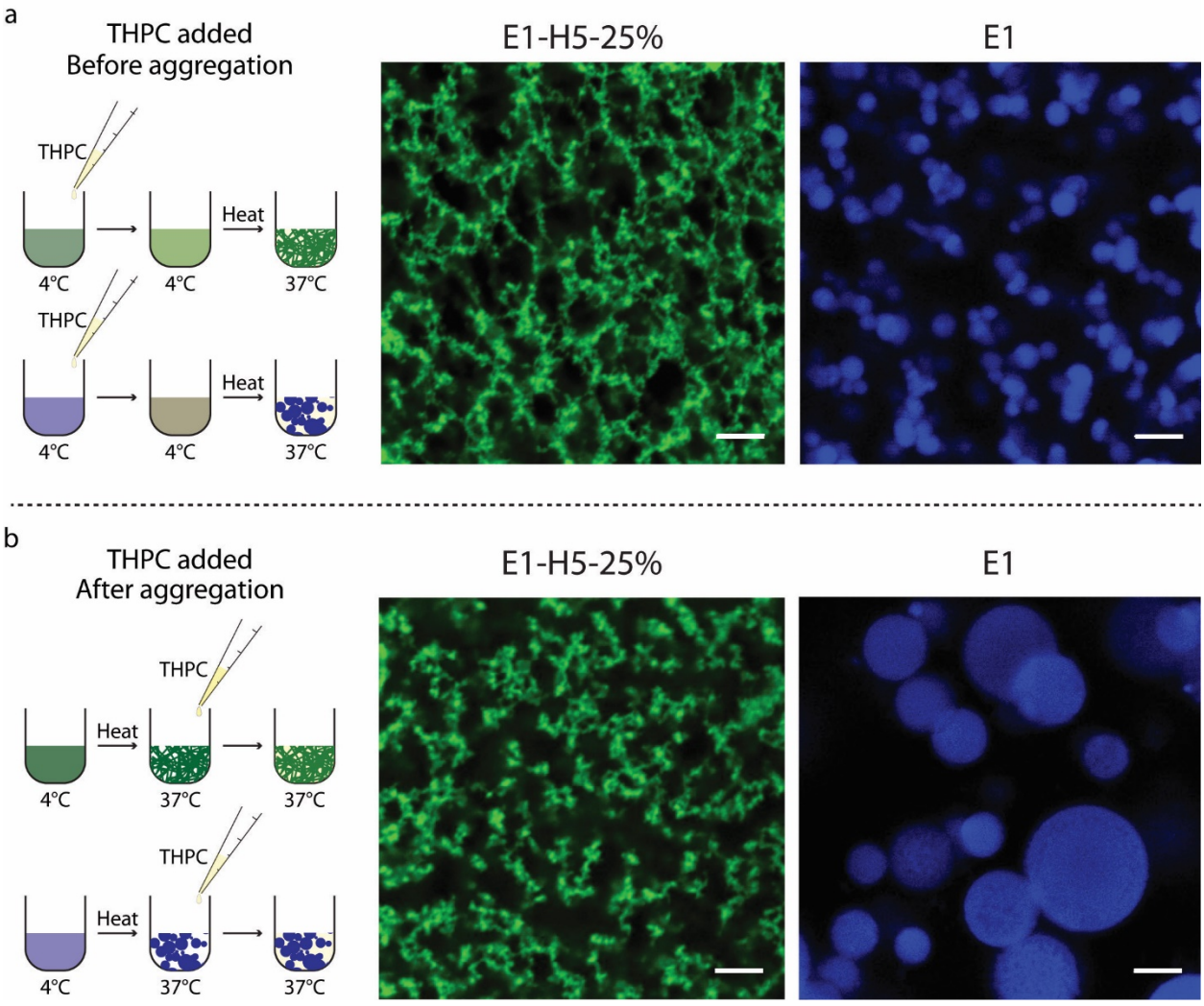

Supplementary Figure 13: POP and ELP architectures with chemical crosslinking (a) When aggregated in the presence of chemical crosslinker—THPC at 1:4 molar ratio (1:1 with present lysines)—$E1_{80}DK$, sequentially identical to E1 with D's and K's spaced as on E1-H5, undergoes liquid-like coacervation. When those coacervates interact with one another, they covalently attach, producing a snapshot in time of coalescence. The presence of crosslinker during POP aggregation has little effect on the observed architecture; it forms an interpercolated network of entangled polymers (with coacervate size locking at the mesoscale as observed with SIM). (b) Architectural differences are even more striking if the crosslinker is added 5 minutes after aggregation has occurred. The POP architecture is similar, though the ELP coacervates are much larger as they were given more time to coalesce. All polymers are at 800μM in PBS. All scale bars 5 μm.

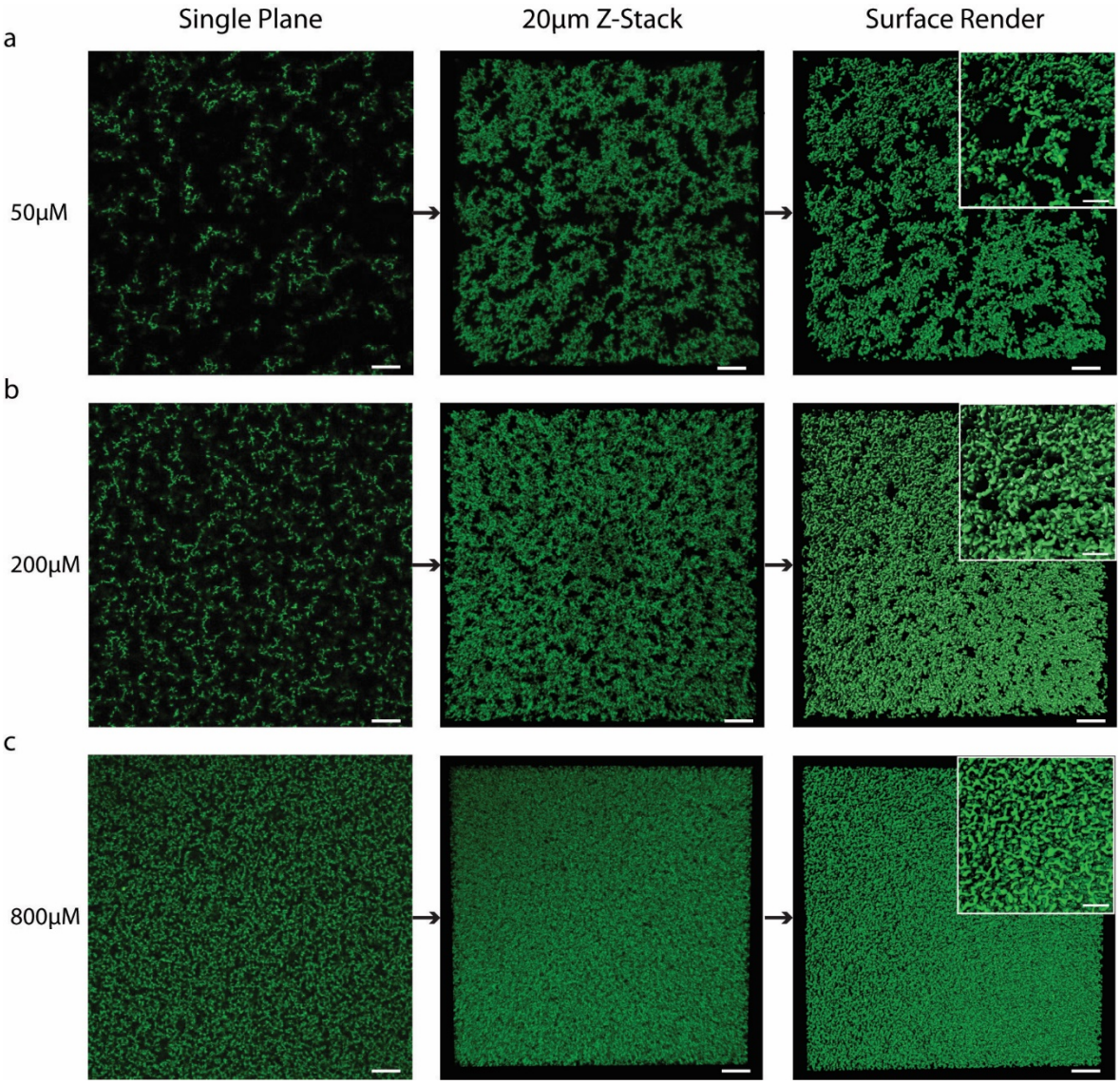

Supplementary Figure 14: Confocal microscopy analysis of POPs Representative single z-slices, 20 µm z-stacks, and IMARIS surface renders of those same z-stacks (including magnified insets) are provided for E1-H5-25% at (a) 50 µM, (b) 200 µM, and (c) 800 µM. 20µm z-stacks can be qualitatively compared; however, all quantitative analysis was done with rendered networks as described in the supplementary methods. Scale bars = 2 µm; scale bars in insets = 10 µm.

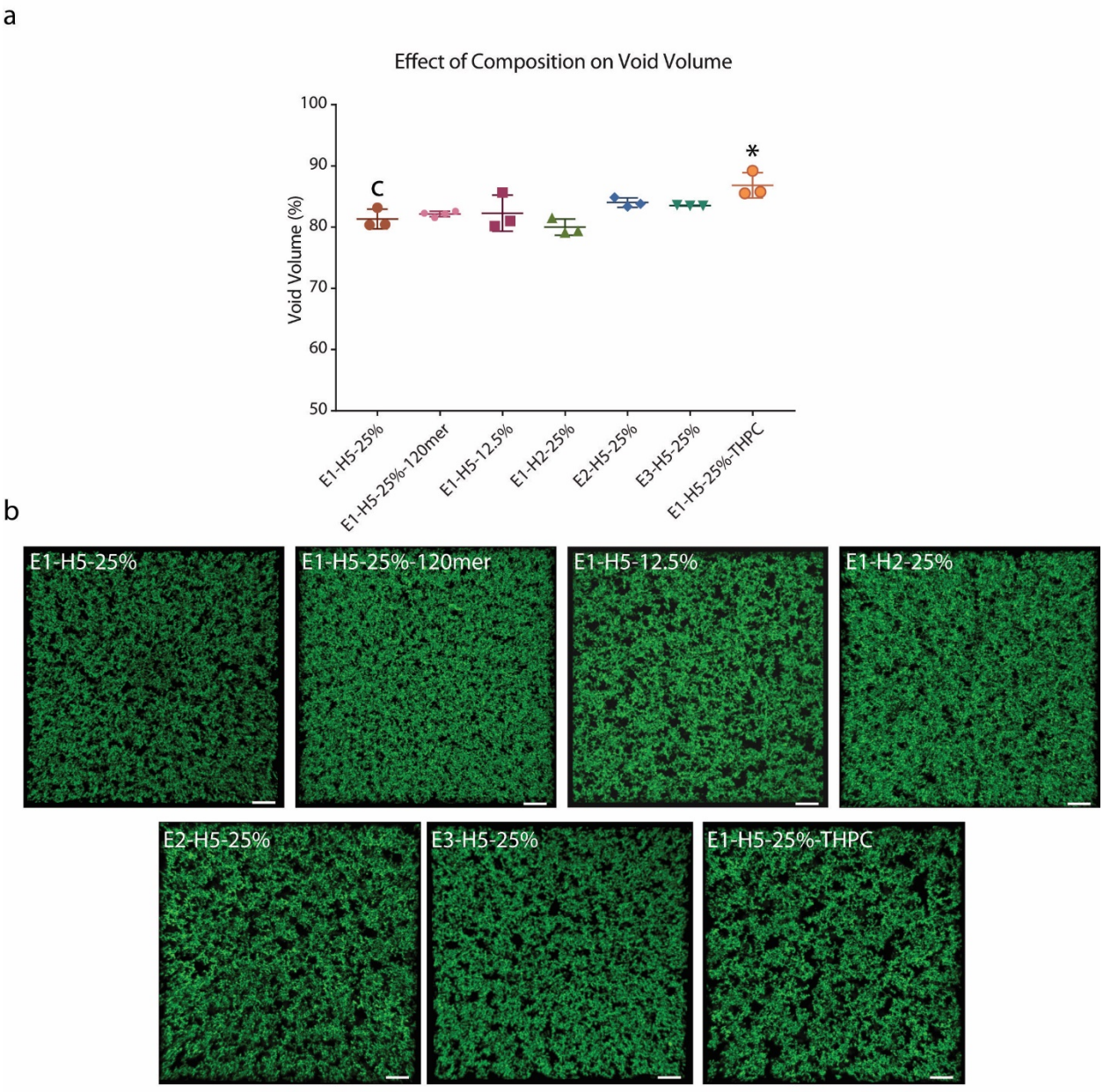

Supplementary Figure 15: Void volume and composition (a) Though composition has controllable effects on stimuli-responsive and mechanical properties, it is largely unaffected by composition. Similar porosities were observed for all tested polymer compositions (200 μM, PBS), though the inclusion of a chemical cross-linker did have a slight, significant effect; * for $p<0.05$ determined by ANOVA with a Dunnett's post hoc test comparing each to E1-H5-25% as a control ('C'); data are presented as 10-90% box plots with a median central element (n=3 independent samples). (b) Representative z-stacks (20 μm thick) are shown for each tested composition. Scale bars = 20 μm.

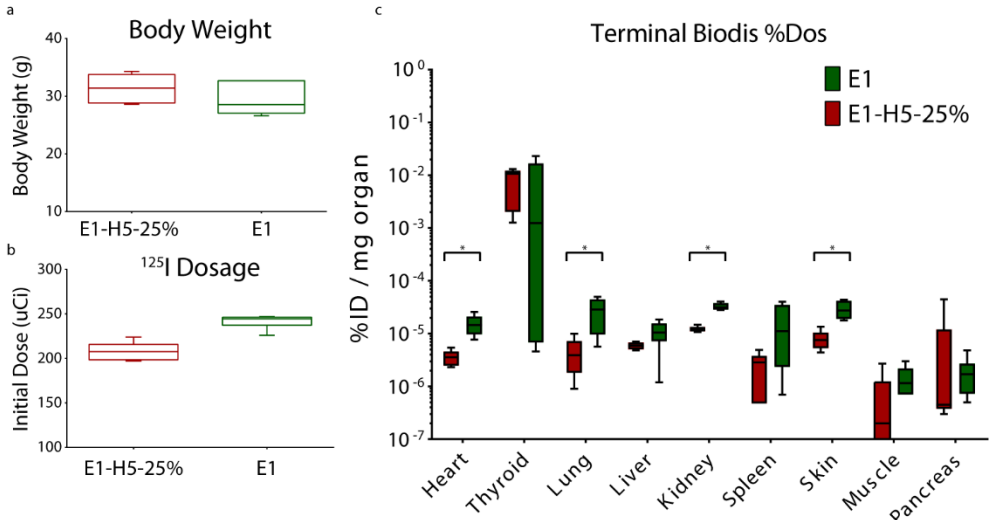

Supplementary Figure 16: Biodistribution of POPs (a) Body weight measures for all mice used are given along with the (b) dose of ^{125}I for each group. Dosages were used for data normalization and differences in doses on reflect an increase in bound iodine for POPs which is not expected to be experimentally relevant. (c) Radiation measured for organs after 120hrs reveals some small distribution differences for POPs and ELPs, but none expected to be harmful; * for $p<0.05$ determined by separate two-tailed t-tests; data are presented as 10-90% box plots with a median central element (n=6 mice).

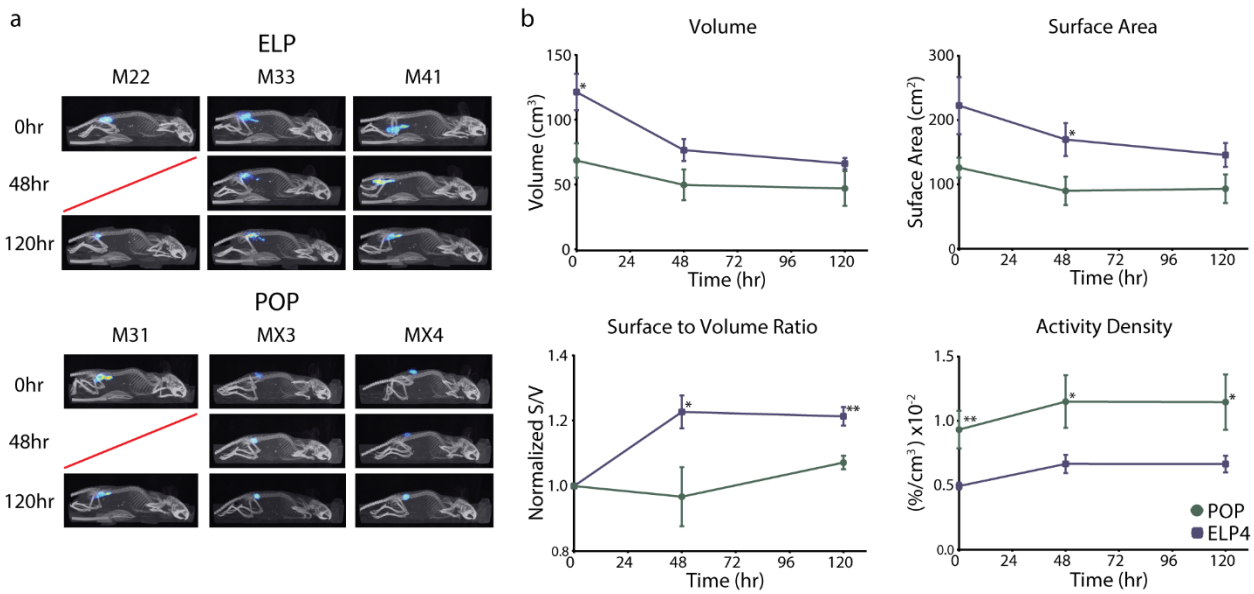

Supplementary Figure 17: SPECT-CT analysis (a) SPECT-CT images are shown for the three mice imaged for SPECT analysis (M22 and M31 48hour CT images failed to output). (b) Injected ELPs show higher volumes, higher surface areas, higher S/V ratios, and a lower percentage of injected dose per unit volume than injected POPs. Due to small n, statistical significance was only achieved in some cases; *p<0.1 and **p<0.05 as determined by repeated measures ANOVA (n=3 mice).

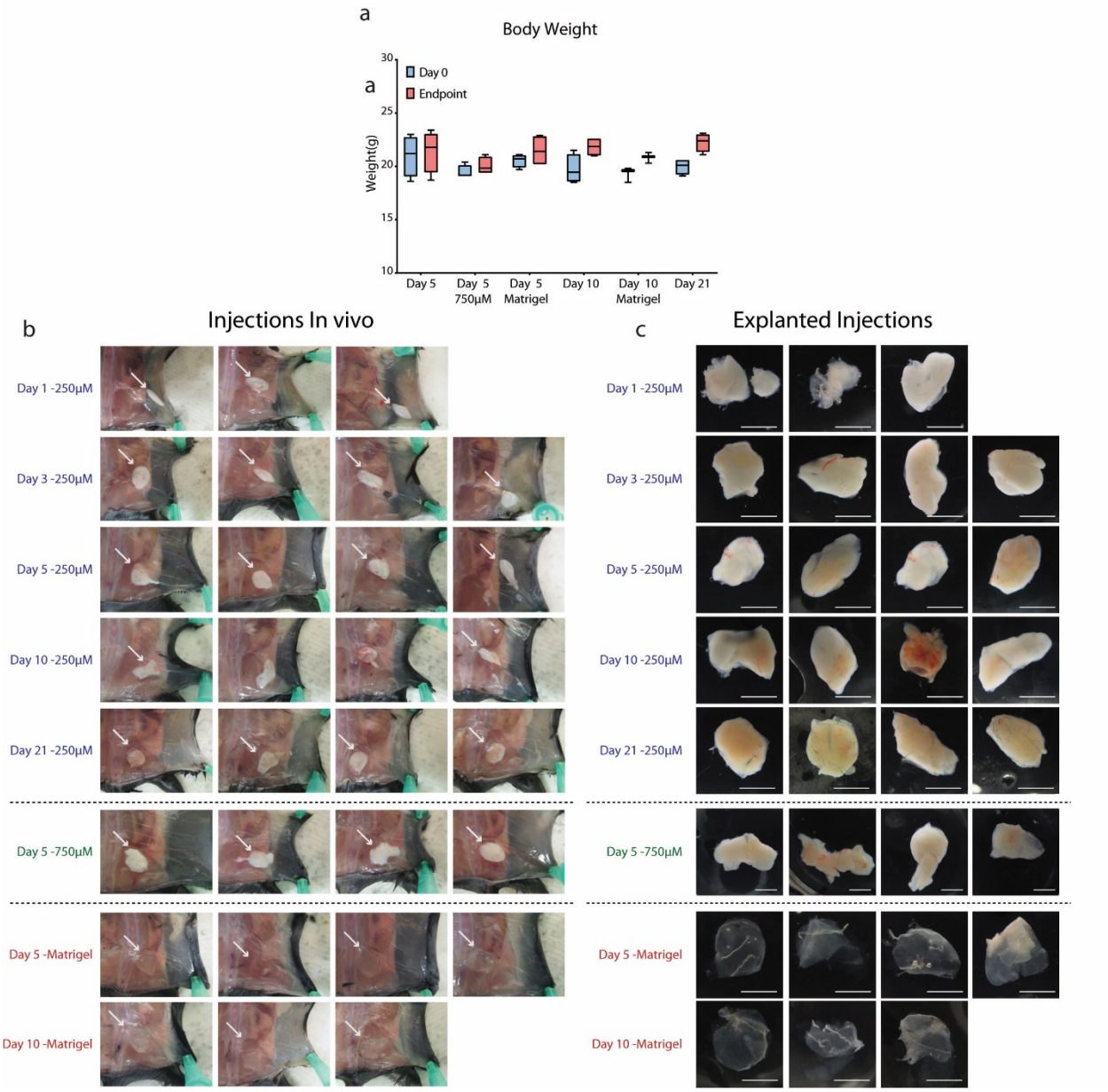

Supplementary Figure 18: Excised depots (a) Mice did not significantly change body weight across time points (day 1 and 3 not collected); data are presented as 10-90% box plots with a median central element (D10 Matrigel n=3, remaining n=4 mice). POP (E1-H5-25%-120) and Matrigel depots are shown (b) pre-and (c) post-excision from the subcutaneous right flank. Scale bars = 5mm.

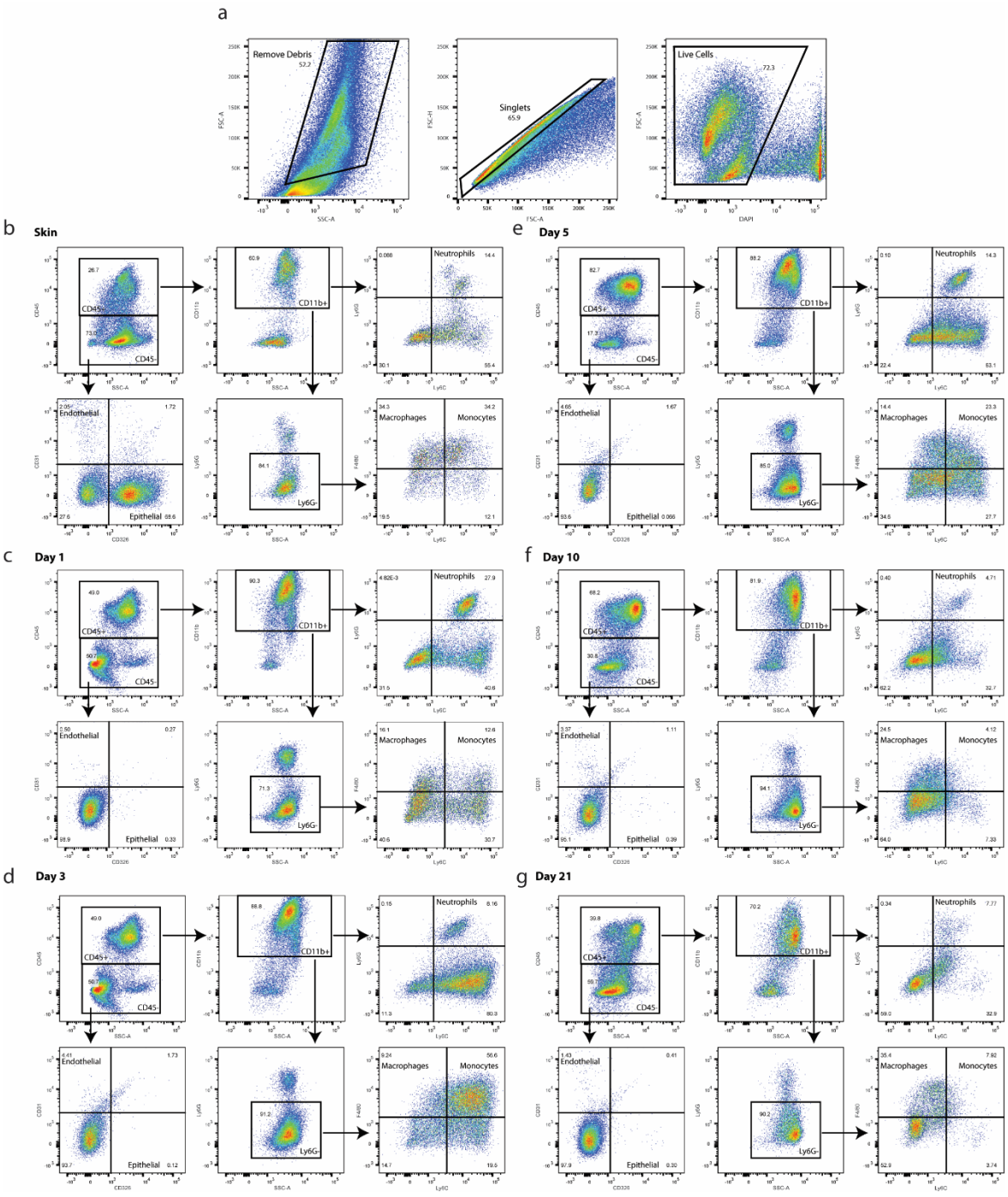

Supplementary Figure 19: Flow cytometry gates for 250 µM POP (a) Gates for removing cell debris and isolating singlets and live cells are shown. (b-g) Flow cytometry gating procedures to isolate all cell types are shown with examples from each time point for 250µM POP samples. Cell subtypes are described in more detail in the supplementary methods.

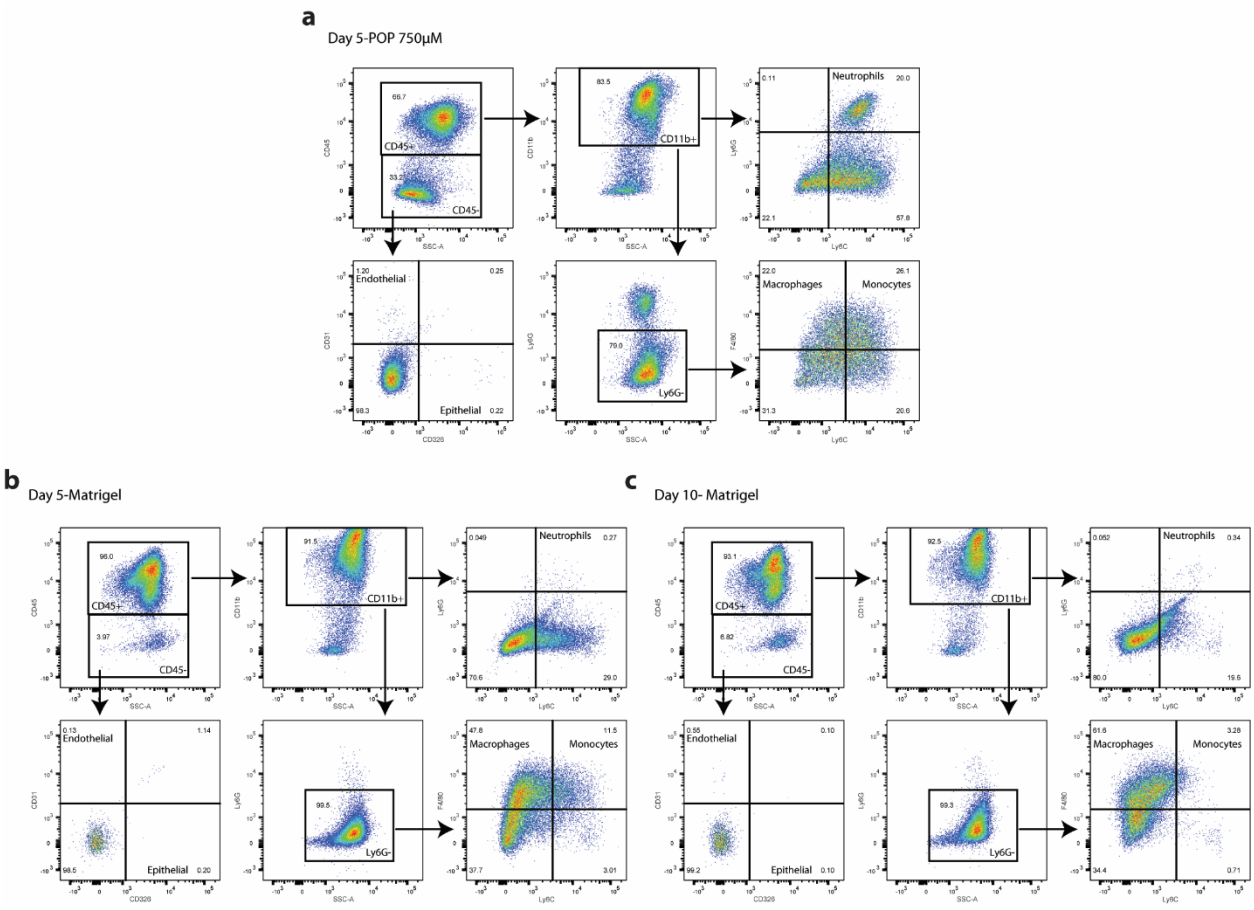

Supplementary Figure 20: Flow gates for comparison groups (all) Additional example flow gates are shown for (a) Day 5 750 µM E1-H5-25%-120 and (b-c) Matrigel.

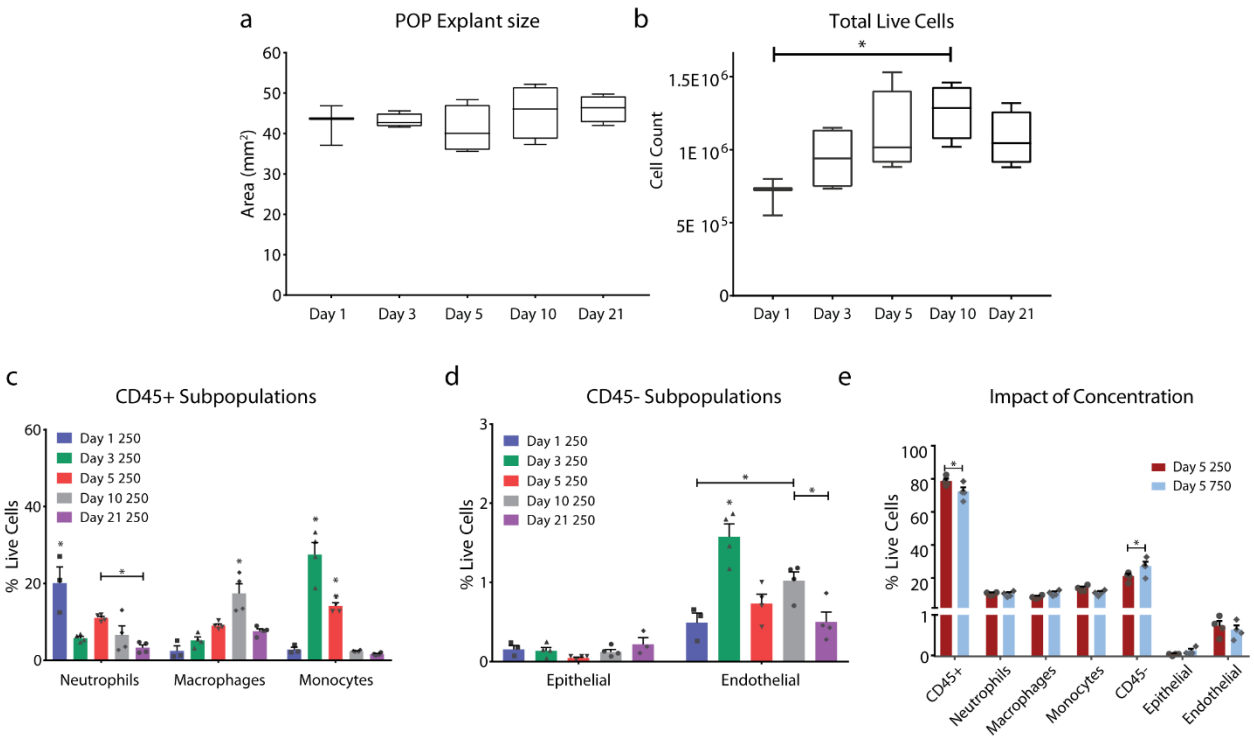

Supplementary Figure 21: Additional cell subtype analysis (a) There was not a significant change in the 250 µM POP (E1-H5-25%-120) subcutaneous injection sizes across all time points, though (b) total live cells did increase; *, $p<0.05$ determined by ANOVA with Tukey post hoc; data are presented as 10-90% box plots with a median central element (D1 n=3, D3-21 n=4 mice). (c) CD45+ subtypes for 250 µM POPs show an initial spike in neutrophils, followed by monocytes and finally macrophages. (d) Epithelial cells and endothelial cells show little to no trend. For c,d, * for $p<0.05$ as determined by ANOVA with Tukey post hoc (D1 n=3, D3-21 n=4 mice). (e) At day 5, the 250 µM and 750 µM POP groups were almost identical, with some slight change in the CD45+/- populations. * for $p<0.05$ determined by two-tailed t-tests (n=4 mice).

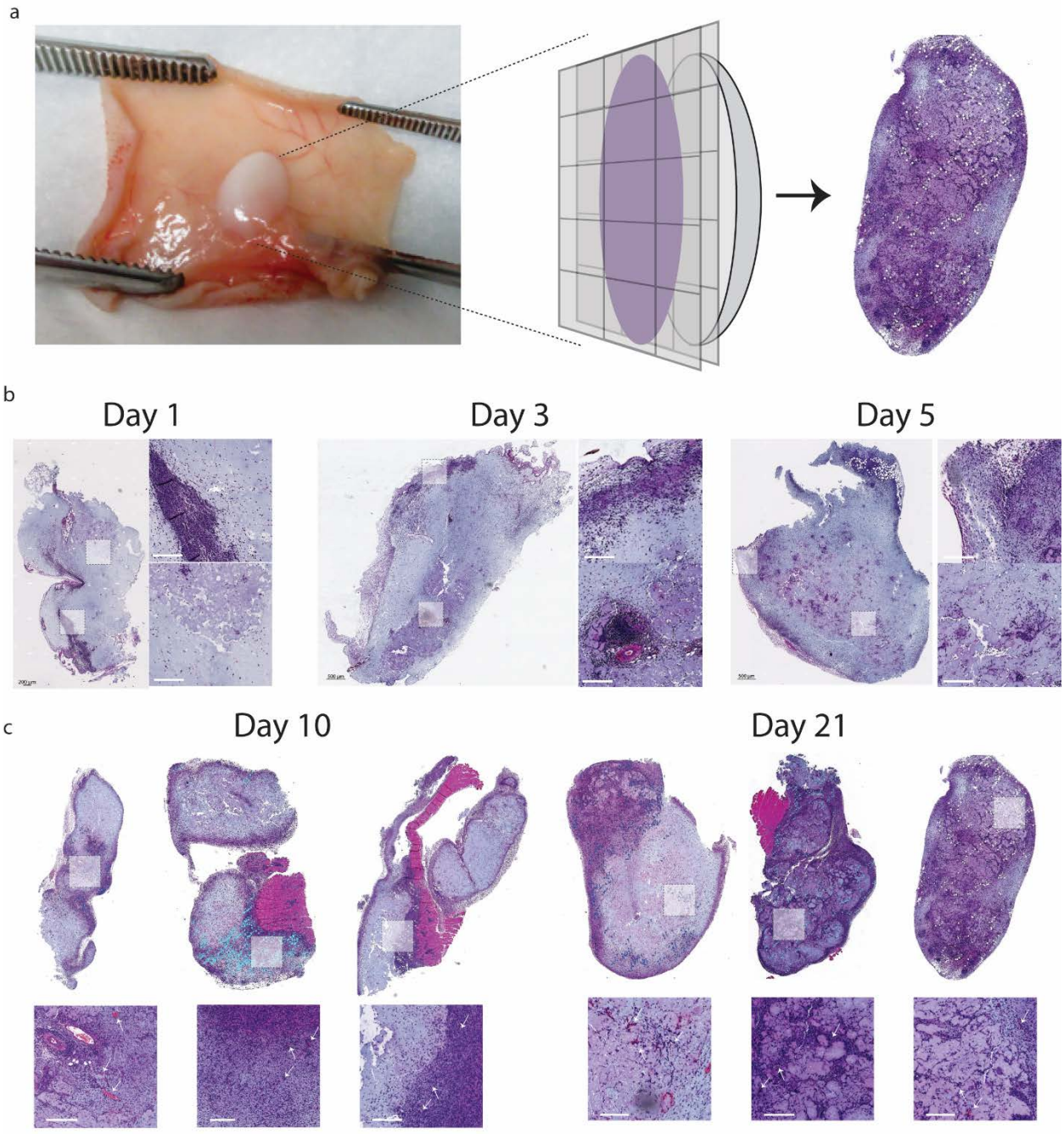

Supplementary Figure 22: Additional histological analysis (a) Histological slices for explanted E1-H5-25%-120 injections were collected from the center of the depots and stained with Hematoxylin and Eosin (H&E). (b) Representative slices for days 1-5 show cells present in the depots from day 1 with a visible increase in density over time. Cells primarily migrate from surrounding tissue (also note in c), but some denser internal regions can also be seen by day 5. (c) H&E stained slices from day 10 and day 21 show a continued increase in cell density and the emergence of vasculature. Colored dots (and arrows) on the slices indicate the presence of blood vessels or capillaries. At day 10, the vasculature is denser around the edges, near surrounding tissue, but it becomes more uniformly distributed by day 21. Scale bars for all zoomed images = 200μm. Of note, chronic inflammatory markers such as foreign body giant cells and the formation of thick fibrin capsules were not observed in any of the stained sections.

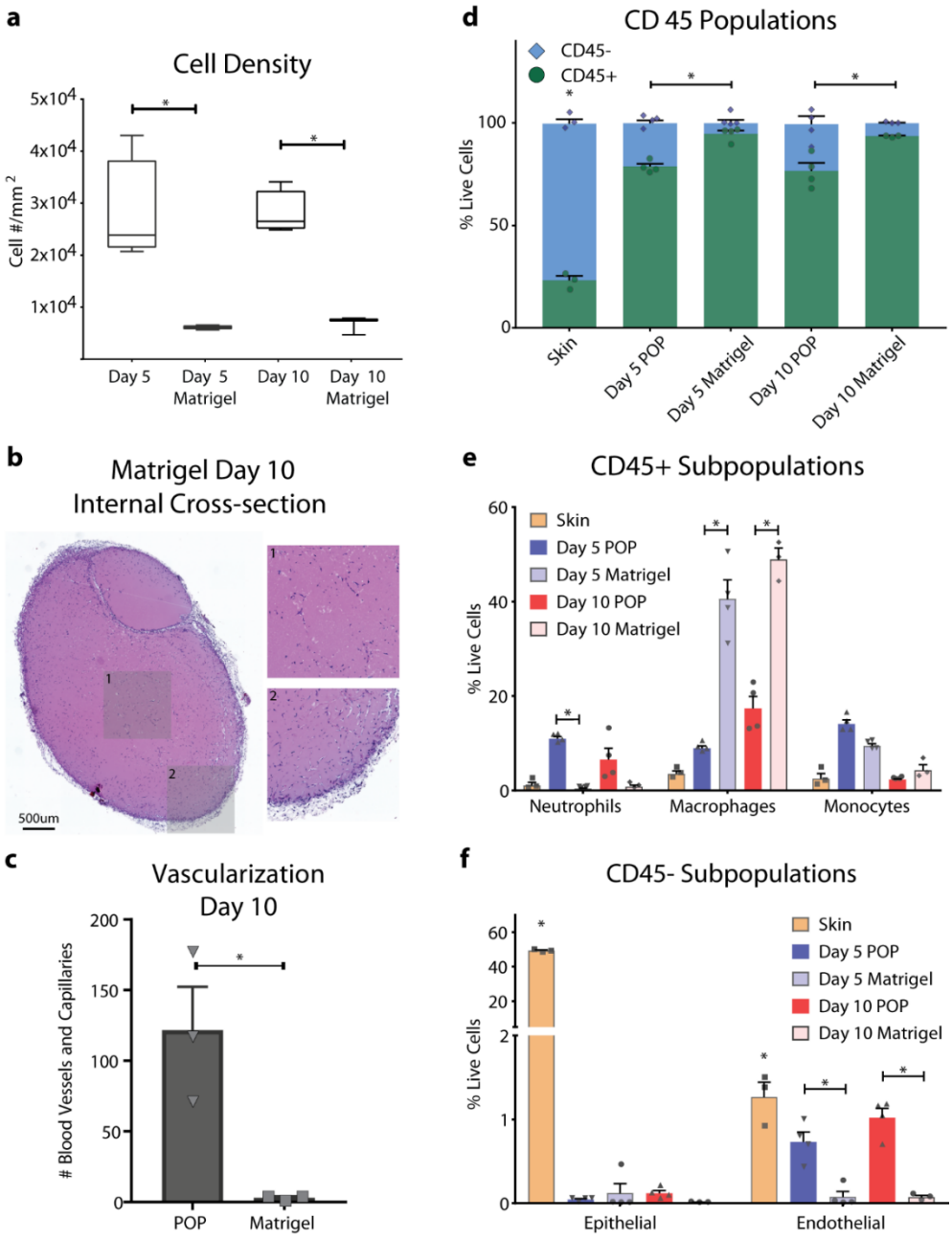

Supplementary Figure 23: Comparison to Matrigel (a) POPs recruit significantly more cells at day 5 and day 10; * for $p<0.05$ determined by two-tailed t-tests (n=4 mice); data are presented as 10-90% box plots with a median central element (POP n=4, Mat n=3 mice). (b) An H&E stained Matrigel sample at Day 10 shows minimal cell recruitment and no vascularization. (c) POP shows significantly increase vascularization at day 10 (n=3); * for $p<0.05$ determined by two-tailed t-tests (n=3 independent slices). (d) POPs recruit more non-hematopoietic cells, (e) more neutrophils, fewer macrophages, and (f) more endothelial cells than Matrigel; for *, $p<0.05$ determined by ANOVA with Tukey post hoc; data means ± SEM (POP n=4, MAT n=3 mice).

Supplementary Tables:

Supplementary Table 1: Polymer sequences and molecular weight

Polymer	Sequence	MW (kDa)
$(E1)_{80}$	$(VPGVG)_{80}$	33.2
$(E2)_{80}$	$(VPG[A_1/V_4]G)_{80}$	32.8
$(E3)_{80}$	$(VPG[A_1/V_1]G)_{80}$	32.1
$(E1)DK_{80}$	$[(VPGVG)_{15}D(VPGVG)_5K]_4$	34.2
E1-H1-6.25%	$(VPGVG)_{75}$-$G(A)_{25}$	33.0
E1-H1-12.5%	$[(VPGVG)_{35}$-$G(A)_{25}]_2$	32.8
E1-H1-25%	$[(VPGVG)_{15}$-$G(A)_{25}]_4$	32.4
E1-H2-12.5%	$[(VPGVG)_{35}$-$GK(A)_{25}K]_2$	33.3
E1-H2-25%	$[(VPGVG)_{15}$-$GK(A)_{25}K]_4$	33.4
E1-H2-50%	$[(VPGVG)_5$-$GK(A)_{25}K]_8$	33.6
E1-H3-12.5%	$[(VPGVG)_{35}$-$G(KAAAA)_5K]_2$	33.6
E1-H3-25%	$[(VPGVG)_{15}$-$G(KAAAA)_5K]_4$	34.0
E1-H5-6.25%	$(VPGVG)_{75}$-$GD(A)_{25}K$	33.2
E1-H5-12.5%	$[(VPGVG)_{35}$-$GD(A)_{25}K]_2$	33.3
E1-H5-25%	$[(VPGVG)_{15}$-$GD(A)_{25}K]_4$	33.4
E1-H5-25%-40mer	$[(VPGVG)_{15}$-$GD(A)_{25}K]_2$	16.9
E1-H5-25%-120mer	$[(VPGVG)_{15}$-$GD(A)_{25}K]_6$	49.8
E2-H5-25%	$[(VPG[A_1/V_4]G)_{15}$-$GD(A)_{25}K]_4$	33.0
E3-H5-25%	$[(VPG[A_1/V_1]G)_{15}$-$GD(A)_{25}K]_4$	34.1

*A Met leader and Gly-Try-Pro trailer are also include on all polymers

Supplementary Table 2: CD Predictions

Polymers	Helix (%)	Beta Sheet (%)	Turn (%)	Disorder (%)
$(ELP1)_{80}$	1.6	23.9	14.8	59.7
ELP1-H1-25%	47	13.7	6.1	33.2
ELP1-H2-25%	35.8	34.5	0.3	29.4
ELP1-H3-25%	27.5	44.9	0	27.6
ELP1-H5-25%	40.1	16.8	6.5	36.6
ELP1-H5-12.5%	19.4	32.1	4.4	44.1

Supplementary Table 3: NMR peak predicted helicity and temperature shift coefficients

Peak	Helicity*	Coefficient (ppb/K)**
1	93.0%	-19.6
2	91.9%	-20.8
3	90.9%	-20.7
4	89.4%	-24.2
5	86.0%	-25.7
6	84.1%	-29.1
7	79.7%	-30.3

*determined for H2 at 20˚C based on chemical shifts at 15˚C

**^{13}C in H(N)CO spectra

Supplementary Table 4: DNA Cassettes for Pre-RDL

E1	Forward	TGTGGGTGTTCCGGGCGTAGGTGTCCCAGGTGTGGGCGTACCGGGCGT TGGTGTTCCTGGTGTCGGCGTGCCGGG
	Reverse	CGGCACGCCGACACCAGGAACACCAACGCCCGGTACGCCCACACCTGG GACACCTACGCCCGGAACACCCACACC
E2	Forward	CGTGGGTGTTCCGGGCGTAGGTGTCCCAGGTGCGGGCGTACCGGGCGT TGGTGTTCCTGGTGTCGGCGTGCCGGG
	Reverse	CGGCACGCCGACACCAGGAACACCAACGCCCGGTACGCCCGCACCTGG GACACCTACGCCCGGAACACCCACGCC
E3	Forward	CGCCGGAGTGCCAGGCGTGGGTGTTCCAGGAGCAGGCGTTCCAGGTGT GGGTGTTCCTGG
	Reverse	AGGAACACCCACACCTGGAACGCCTGCTCCTGGAACACCCACGCCTGG CACTCCGGCGCC
H1	Forward	TGCGGCCGCAGCTGCGGCGGCAGCCGCGGCTGCCGCGGCTGCAGCGGC AGCCGCGGCTGCGGCGGCCGCAGCTGCGGG
	Reverse	CGCAGCTGCGGCCGCCGCAGCCGCGGCTGCCGCTGCAGCCGCGGCAGC CGCGGCTGCCGCCGCAGCTGCGGCCGCACC
H2	Forward	TAAAGCGGCCGCAGCTGCGGCGGCAGCCGCGGCTGCCGCGGCTGCAGC GGCAGCCGCGGCTGCGGCGGCCGCAGCTGCGAAAGG
	Reverse	TTTCGCAGCTGCGGCCGCCGCAGCCGCGGCTGCCGCTGCAGCCGCGGC AGCCGCGGCTGCCGCCGCAGCTGCGGCCGCTTTACC
H3	Forward	TAAAGCGGCCGCAGCTAAAGCCGCGGCAGCGAAAGCAGCCGCGGCGA AAGCCGCAGCTGCGAAAGCGGCAGCCGCGAAGGG
	Reverse	CTTCGCGGCTGCCGCTTTCGCAGCTGCGGCTTTCGCCGCGGCTGCTTTC GCTGCCGCGGCTTTAGCTGCGGCCGCTTTACC
H5	Forward	TGATGCGGCCGCAGCTGCGGCGGCAGCCGCGGCTGCCGCGGCTGCAGC GGCAGCCGCGGCTGCGGCGGCCGCAGCTGCGAAAGG
	Reverse	TTTCGCAGCTGCGGCCGCCGCAGCCGCGGCTGCCGCTGCAGCCGCGGC AGCCGCGGCTGCCGCCGCAGCTGCGGCCGCATCACC

*Note that H4, $K(AAALA)_5K$, was initially cloned but did not express sufficiently to warrant inclusion in the manuscript

Supplementary References

1 Micsonai, A. *et al.* Accurate secondary structure prediction and fold recognition for circular dichroism spectroscopy. *Proc Natl Acad Sci U S A* **112**, E3095-3103, doi:10.1073/pnas.1500851112 (2015).

2 Sreerama, N. & Woody, R. W. Estimation of protein secondary structure from circular dichroism spectra: comparison of CONTIN, SELCON, and CDSSTR methods with an expanded reference set. *Anal Biochem* **287**, 252-260, doi:10.1006/abio.2000.4880 (2000).

3 Hennessey, J. P. & Johnson, W. C. Information content in the circular dichroism of proteins. *Biochemistry* **20**, 1085-1094, doi:10.1021/bi00508a007 (2002).

4 Delaglio, F. *et al.* NMRPipe: A multidimensional spectral processing system based on UNIX pipes. *Journal of Biomolecular NMR* **6**, doi:10.1007/bf00197809 (1995).

5 De Simone, A., Cavalli, A., Hsu, S. T., Vranken, W. & Vendruscolo, M. Accurate random coil chemical shifts from an analysis of loop regions in native states of proteins. *J Am Chem Soc* **131**, 16332-16333, doi:10.1021/ja904937a (2009).

6 Camilloni, C., De Simone, A., Vranken, W. F. & Vendruscolo, M. Determination of secondary structure populations in disordered states of proteins using nuclear magnetic resonance chemical shifts. *Biochemistry* **51**, 2224-2231, doi:10.1021/bi3001825 (2012).

7 Muñoz, V. & Serrano, L. Elucidating the folding problem of helical peptides using empirical parameters. *Nature Structural Biology* **1**, 399-409, doi:10.1038/nsb0694-399 (1994).

8 Lacroix, E., Viguera, A. R. & Serrano, L. Elucidating the folding problem of alpha-helices: local motifs, long-range electrostatics, ionic-strength dependence and prediction of NMR parameters. *J Mol Biol* **284**, 173-191, doi:10.1006/jmbi.1998.2145 (1998).

9 Harmon, T. S., Holehouse, A. S., Rosen, M. K. & Pappu, R. V. Intrinsically disordered linkers determine the interplay between phase separation and gelation in multivalent proteins. *eLife* **6**, e30294 (2017).

10 Ruff, K. M., Harmon, T. S. & Pappu, R. V. CAMELOT: A machine learning approach for coarse-grained simulations of aggregation of block-copolymeric protein sequences. *Journal of Chemical Physics* **143**, 243123, doi:10.1063/1.4935066 (2015).

11 Vitalis, A. & Pappu, R. V. ABSINTH: A New Continuum Solvation Model for Simulations of Polypeptides in Aqueous Solutions. *Journal of Computational Chemistry* **30**, 673-699, doi:10.1002/jcc.21005 (2009).

12 Radhakrishnan, A., Vitalis, A., Mao, A. H., Steffen, A. T. & Pappu, R. V. Improved Atomistic Monte Carlo Simulations Demonstrate That Poly-L-Proline Adopts Heterogeneous Ensembles of Conformations of Semi-Rigid Segments Interrupted by Kinks. *Journal of Physical Chemistry B* **116**, 6862-6871, doi:10.1021/jp212637r (2012).

13 Lyle, N., Das, R. K. & Pappu, R. V. A quantitative measure for protein conformational heterogeneity. *The Journal of Chemical Physics* **139**, 121907, doi:10.1063/1.4812791 (2013).

14 Das, R. K., Ruff, K. M. & Pappu, R. V. Relating sequence encoded information to form and function of intrinsically disordered proteins. *Current Opinion in Structural Biology* **32**, 102-112, doi:http://dx.doi.org/10.1016/j.sbi.2015.03.008 (2015).

15 Chen, J. *et al.* The use of self-adjuvanting nanofiber vaccines to elicit high-affinity B cell responses to peptide antigens without inflammation. *Biomaterials* **34**, 8776-8785, doi:10.1016/j.biomaterials.2013.07.063 (2013).

16 Trabbic-Carlson, K., Setton, L. A. & Chilkoti, A. Swelling and mechanical behaviors of chemically cross-linked hydrogels of elastin-like polypeptides. *Biomacromolecules* **4**, 572-580, doi:10.1021/bm025671z (2003).
17 Lim, D. W., Nettles, D. L., Setton, L. A. & Chilkoti, A. Rapid cross-linking of elastin-like polypeptides with (hydroxymethyl)phosphines in aqueous solution. *Biomacromolecules* **8**, 1463-1470, doi:10.1021/bm061059m (2007).
18 Madl, C. M., Katz, L. M. & Heilshorn, S. C. Bio-Orthogonally Crosslinked, Engineered Protein Hydrogels with Tunable Mechanics and Biochemistry for Cell Encapsulation. *Adv Funct Mater* **26**, 3612-3620, doi:10.1002/adfm.201505329 (2016).
19 Sallach, R. E. *et al.* Elastin-mimetic protein polymers capable of physical and chemical crosslinking. *Biomaterials* **30**, 409-422, doi:10.1016/j.biomaterials.2008.09.040 (2009).